PERMAFROST AND PERIGLACIAL PROCESSES
Permafrost and Periglac. Process. (2017)
Published online in Wiley Online Library
(wileyonlinelibrary.com) DOI: 10.1002/ppp.1944

Utilising a Suite of Isotopic and Elemental Tracers to Constrain Cryoturbation Rates and Patterns in a Non-sorted Circle

Nicolas A. Jelinski,[1]* *Kyungsoo Yoo*[1] *and Jonatan Klaminder*[2]

[1] Department of Soil, Water and Climate, University of Minnesota–Twin Cities, Saint Paul, Minnesota USA
[2] Department of Ecology and Environmental Sciences, Umea University, Umea, Sweden

ABSTRACT

The empirical quantification of rates of material movement in cryoturbated soils has lagged behind the physical and chemical characterisation of these materials. We applied a novel suite of elemental (C, Hg), stable isotope (^{13}C) and radioisotope (^{137}Cs, ^{210}Pb, ^{14}C, ^{10}Be) tracers in conjunction with analytical and numerical models to constrain the rates and patterns of soil movement due to cryoturbation in a non-sorted circle (NSC) near Abisko, Sweden. We present the first observations of the variability of ^{10}Be across a patterned-ground feature, which facilitate the interpretation of subsurface peaks in soil organic carbon, Hg and ^{13}C and provide constraints on the surficial histories of cryoturbated materials. Apparent rates of surficial lateral movement across the NSC estimated from ^{137}Cs and ^{210}Pb (0–2.55 cm year^{-1}) decreased with distance from its centre and were an order of magnitude greater than rates of subduction and subsurface movement estimated from ^{14}C (0.04–0.27 cm year^{-1}). Novel estimates of the original surficial residence times of cryoturbated parcels based on excess ^{10}Be and Hg inventories ranged from 238 to 3940 years. Our results demonstrate the utility of the spatially explicit application of elemental and radioisotopic tracer suites to constrain cryoturbation rates in Arctic patterned ground. Copyright © 2017 John Wiley & Sons, Ltd.

KEY WORDS: cryoturbation; non-sorted circle; ^{10}Be; ^{14}C; ^{137}Cs; ^{210}Pb

INTRODUCTION

Recent estimates of permafrost soil organic carbon (SOC) stocks to 3 m depth place 35–44 per cent of global SOC in cryoturbated soils (Tarnocai *et al.,* 2009; Hugelius *et al.,* 2014). Global-scale models of soil carbon accumulation in permafrost-affected soils suggest that the effects of both cryoturbation and the insulation of the soil surface by organic materials can result in 30 per cent higher stocks of SOC in the top 1 m, with additional increases down to 3 m (Koven *et al.,* 2009). Other evidence suggests that the rates at which organic materials are buried and frozen through cryoturbation may result in differences in long-term behaviour with regard to decomposition potential and lability (Xu *et al.,* 2009; Koven *et al.,* 2011). Despite this importance, the empirical quantification of rates of material movement in cryoturbated soils has lagged far behind the physical and chemical characterisation of these materials (Bockheim, 2007; Koven *et al.,* 2011).

The measurement and modelling of the physical mechanisms and biogeochemical effects of cryoturbation have been well studied in non-sorted circles (NSCs). This type of patterned ground is ubiquitous across Arctic ecosystems, occurs in regular spatial patterns, and exhibits strikingly similar morphologies and patterning with regard to vertical and horizontal distributions of SOC, relative depth to permafrost table, and temperature gradients (Walker *et al.,* 2004; Nicolsky *et al.,* 2008; Ping *et al.,* 2008). In the 'equilibrium cell' model of cryoturbation in NSCs and related forms of patterned ground (including hummocks and sorted circles), three major mechanisms drive the overall pattern of material movement (Figure 1): (i) differential frost heave due to accelerated movement of the freezing front through the non-vegetated centre leads to the formation of ice lenses and reinforcement of microtopography; (ii) colluvial or co-alluvial movement of material from the NSC centre towards the edges; and (iii) the subduction or frost-churning of large, intact parcels of surface organic

* Correspondence to: N. A. Jelinski, Department of Soil, Water and Climate, University of Minnesota-Twin Cities, 1991 Upper Buford Circle, Saint Paul, MN 55108, USA. E-mail: jeli0026@umn.edu

Contract/grant sponsor: National Science Foundation; contract/grant number: EAR-1253198.
Contract/grant sponsor: Swedish Research Council; contract/grant number: Project No. 2009-3282.

Received 20 March 2016
Revised 20 December 2016
Accepted 25 January 2017

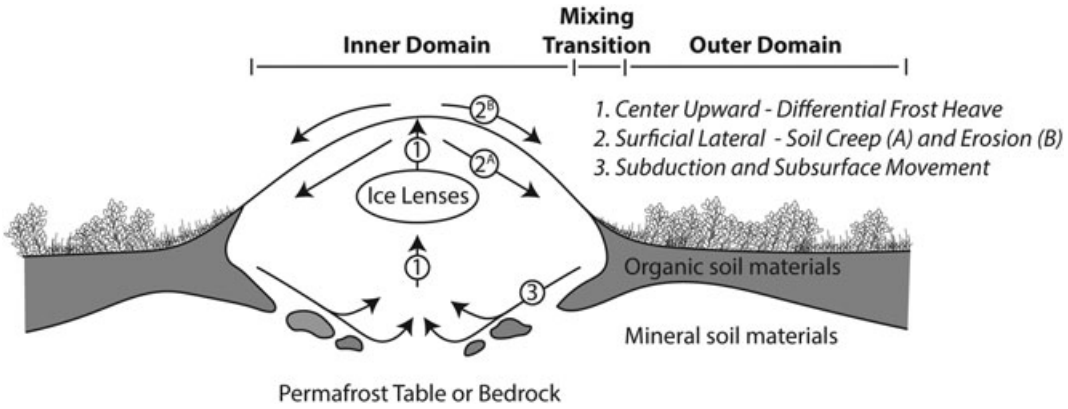

Figure 1 Idealised diagram of vertical cross section through a non-sorted circle, showing the spatial relationship of organic (grey) and mineral (white) soil materials, domain terminology, physical movement processes and hypothesised directions of soil movement (adapted from Klaminder *et al.,* 2014).

material downward towards (and eventually along) the permafrost table (Mackay, 1980; Hallet and Prestrud, 1986; Nicolsky *et al.,* 2008; Ping *et al.,* 2015). The net movement of materials in NSCs is therefore hypothesised to be a complex pseudo-circular pattern that can be idealised with several major components (Figure 1). The most critical factor in moving material in these features is differential frost heave, which creates and maintains microtopographic gradients (Peterson and Krantz, 2003).

Previous work has estimated the rate of soil movement by freeze–thaw processes in NSCs and other types of patterned ground by tracking positioning changes in physical markers (Egginton and Shilts, 1978; Smith, 1986; Hallet *et al.,* 1988; Ballantyne, 1996; Selkirk, 1998; Sawyer, 2007), photogrammetry (Kääb *et al.,* 2013), or using the short-lived radioisotope ^{210}Pb (Hagedorn *et al.,* 2008; Klaminder *et al.,* 2014). However, most of these studies have focused on quantifying rates of surficial movement, with sparse estimates of the patterns or rates of subduction (Harris, 1998; Becher *et al.,* 2013), subsurface movement rates (Dyke and Zoltai, 1980; Hallet *et al.,* 1988) or the surficial history of cryoturbated materials in NSCs.

The objectives of this study were to utilise a comprehensive suite of elemental (C, Hg) stable isotope (^{13}C) and radioisotope (^{137}Cs, ^{210}Pb, ^{14}C, ^{10}Be) tracers to empirically constrain the rates and patterns of material movement in a single NSC over a range of timescales. We report the first spatially explicit measurements of meteoric ^{10}Be across short distances in cryoturbated soils, and demonstrate the potential use of ^{10}Be to reveal the surficial histories of cryoturbated materials.

MATERIALS AND METHODS

Site Description and Soil Sampling

Our study site is a single NSC (1.45 m in radius) located in a larger NSC field on the north slope of Mt Suorooaivi, at an altitude of approximately 700 m a.s.l., 20 km south of the village of Abisko, Sweden (68°18′N, 19°10′E). Within the NSC field, slopes are generally <5 per cent and the soils are formed from thin deposits of Weichselian-aged glacial till over bedrock. The mineral soil is predominantly loam and sandy loam with clay contents ranging from 5 to 21 per cent and silt contents ranging from 32 to 50 per cent (Supporting Information, Appendix S1, Table S2). Deglaciation probably occurred approximately 9000 years BP near Abisko (Lundqvist, 2004). This site has been utilised for investigations into NSC dynamics previously and described by Makoto and Klaminder (2012), Klaus *et al.* (2013), Becher *et al.* (2013) and Klaminder *et al.* (2014). Briefly, the site lies in the zone of discontinuous permafrost, the active layer is >2 m thick and rapid degradation or lowering of the permafrost table has taken place over the past four decades (Becher *et al.,* 2013). Despite this, active soil movement in NSC microforms and seasonal elevation differences indicative of differential frost-heave processes that initiate and maintain NSCs continue to be observed (Klaus *et al.,* 2013; Klaminder *et al.,* 2014).

Soil profiles were sampled in five locations (at 0, 83, 145, 180 and 260 cm) along a 2.6-m radial transect, outward from the NSC centre, using an 8-cm-diameter auger and spade excavation (Figure 2). Profiles were sampled until bedrock was reached (Figure 2). Sampling location 1 (at 0 cm) was termed the mineral centre (CM); location 2 (83 cm) the inner profile (IN); and location 3 (145 cm), at the outer edge of the NSC, where active subduction of surficial materials is hypothesised to occur, the mixing transition (MT). Together, locations CM, IN and MT constitute samples from the *inner domain*, the part of the transect that is included in the NSC microform (Figure 2). Location 4 (180 cm) is in the *outer domain* (part of the non-NSC areas that do not participate in material movement), termed outer domain 1 (OD1), and location 5 (260 cm) is termed outer domain 2 (OD2). The inner domain and outer domain regions are synonymous with 'circle' and 'inter-circle' or 'boil' and 'inter-boil' terminology (see Walker *et al.,* 2004; Ping *et al.,* 2015).

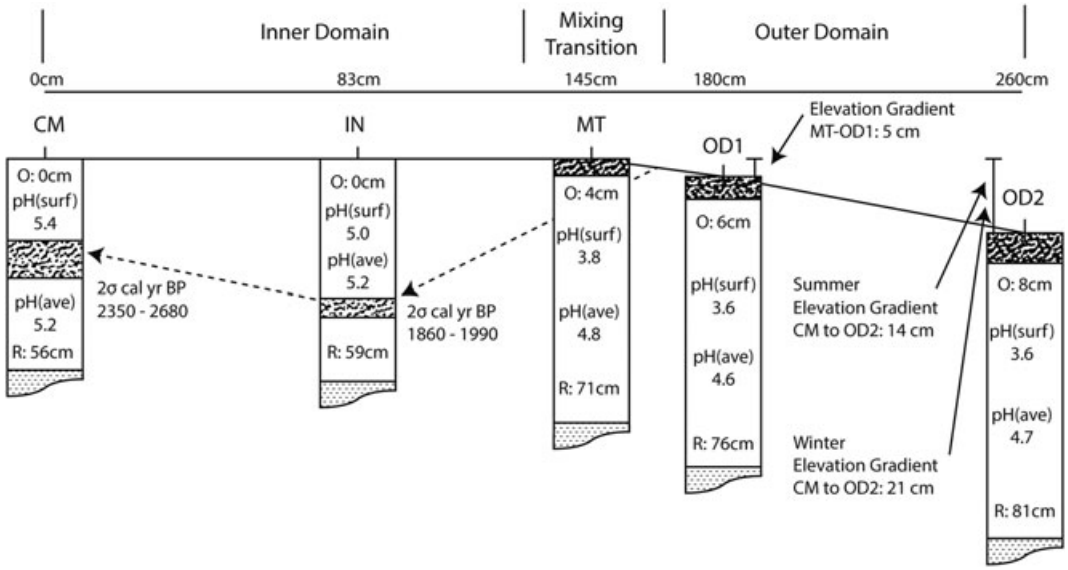

Figure 2 Morphology, characteristics and hypothesised direction of subsurface inner domain material movement (dashed arrows) across the studied non-sorted circle. Surficial (pH surf) and average (pH ave) pH values, organic layer thickness (O) and depth to bedrock (R) are annotated at each sampling point.

Depth to bedrock co-varied with distance from the mineral centre, with observed bedrock depths at 56, 59, 71, 76 and 81 cm, respectively, for sampling locations CM, IN, MT, OD1 and OD2. This result is typical of NSCs near Abisko and, although the morphology may differ slightly from NSCs in deep unconsolidated materials shown in Figure 1, previous work (Becher *et al.,* 2013; Klaminder *et al.,* 2014) has demonstrated that the physical functioning and pattern of material movement of these NSCs may be similarly conceptualised. The materials with the highest thermal conductivities (mineral soil and shallow bedrock) are at the NSC centre and inner domain, while thick organic mats overlie the outer domain, setting up conditions for differential frost heave that drives material movement and circulation (Peterson and Krantz, 2003; Nicolsky *et al.,* 2008).

Soil Chemical Properties

Soil pH was determined on a 1 : 1 soil–water slurry. SOC and total nitrogen were determined on an Elementar varioMax CN analyser, with combustion at 1000°C. Mineral soil texture was determined by the micropipette method (Miller and Miller, 1987), with quality control samples determined by the hydrometer method (Gee and Or, 2002). The concentration of Hg was determined by aqua regia digestion and inductively coupled plasma mass spectrometry. Excess Hg (Hg_{ex}), or atmospherically derived Hg, was calculated by subtracting average Hg concentrations of soils and sediments directly overlying bedrock across the Abisko study site ('inherited Hg') from total Hg concentrations of overlying depth increments. Overviews of the environmental origin and behaviour of the elemental tracers used in this study (as well as the distributions of nine other elements (Pb, S, Cl, N, P, Na, Ca, Mg, K) and additional supporting analysis) can be found in the Supporting Information (Appendix S1, Tables S1, S2, S3, and Figures S1, S4, S5, S6).

Measurements of Radioiostopes (^{14}C, ^{137}Cs, ^{210}Pb, ^{10}Be) and δ^{13}C

Details of the environmental origin and behaviour of the individual isotopic tracers used in our study can be found in Appendix S1. Briefly, the four radioisotopes utilised differ in their half-lives, origins and modes of deposition. Meteoric ^{10}Be is a cosmogenic radioisotope that continuously accumulates at the Earth's surface through wet and dry deposition, with a half-life of 1.39×10^6 years (Willenbring and von Blanckenburg, 2010). ^{14}C is both a cosmogenic and an anthropogenic (derived from atmospheric weapons testing) radioisotope continuously accumulated in soils through plant production, with a half-life of 5730 years (Trumbore, 2009). Both ^{137}Cs and ^{210}Pb are fall-out (wet and dry deposition) radioisotopes with much shorter half-lives; ^{137}Cs is an anthropogenic, pulse deposited isotope (atmospheric weapons testing and nuclear power plant incidents) with a half-life of 30 years, while ^{210}Pb is a geogenic, continuously deposited isotope with a half-life of 22 years (Faure and Mensing, 2005).

Δ^{14}C of bulk SOC (the relative difference between the absolute international standard (base year 1950) and δ^{13}C and age-corrected sample activity) was determined on two cryoturbated samples (IN 37–24 cm and CM 22–32 cm) by AMS analysis on graphite from converted CO_2 produced upon complete sample combustion on acid washed pretreatments of soil samples at Beta Analytical (Miami, FL, USA), using NIST Oxalic Acid I as the modern reference standard. The conventional radiocarbon ages of these samples were calendar calibrated using the IntCal13 database (Reimer *et al.,* 2013).

^{137}Cs was determined by gamma spectrometry on a high-purity germanium (HPGe) crystal well detector (Canberra, Inc., Harwell, UK) at the University of Minnesota – Twin Cities. Samples were counted for 48 h to an uncertainty of 5 per cent of the predicted value. Efficiency calibration of the gamma-spectrometric system was performed using measurement standards outlined by the NIST (Gaithersburg, MD, US).

^{210}Pb activities were determined using alpha spectrometry, which measured the activities of its granddaughter ^{210}Po in equilibrium. ^{210}Po analyses were carried out by the complete dissolution of the aliquot samples (between 150 and 250 mg) by microwave digestion and deposition on silver discs, using ^{209}Po as an internal tracer to determine yield. Polonium sources were measured using an EG & G Ortec ULTRA-AS Ion-Implanted-Silicon Charged-Particle detector (model U-020-450-AS) at Umeå University, Umeå, Sweden. ^{210}Pb in soils comes both from *in situ* decay of Rn in the soil (supported fraction) as well as atmospherically derived ^{210}Pb (unsupported or 'excess' fraction). ^{210}Pb$_{ex}$ was calculated as the difference between the total measured ^{210}Pb activity of every depth increment and the activities measured in the lowermost sampling increment of each sampling location.

Meteoric ^{10}Be adsorbed to mineral grains and bound to organic materials was removed through a series of acidification steps and ion exchange chromatography before being oxidised and analysed by AMS. The methodology used here is modified from Ebert *et al.* (2012). Briefly, 0.5 g of air-dried, homogenised and sieved (2 mm) soil was digested in Teflon vessels with 0.5 M HCl and 250 µg of spiked ^{9}Be carrier at 110°C for 3 h, after which the sediment was removed via centrifugation. Then, 4 ml of HF was added to the cation solution in two steps to bind excess Ca and Mg. After each HF addition step, 2 ml of ultrapure H_2O_2 was added to remove organic material. The ultrapure water containing Be and other cations was removed from the fluoride cake via centrifugation and pipetting. Ion exchange chromatography (both anion and cation removal steps) was used to purify Be cations from the bulk cation solution. Be-hydroxides were precipitated from the purified cation solution by titration to pH 9 through the addition of ammonia. The supernatant was decanted and the precipitate was washed several times with ultrapure water and dried overnight at 100°C in low-boron quartz vials. The dry precipitate was flame-oxidised at >850°C to form BeO powder and pressed into cathodes with niobium powder for AMS analysis at PRIME Lab, Purdue University, USA. A process blank was run with each batch of nine samples.

δ^{13}C of bulk soil samples was determined at the UC Davis Stable Isotope Facility (SIF, Davis, CA, USA). Samples were combusted at 1000°C using an Elementar EL or Micro Cube elemental analyser (Elementar, Hanau, Germany) interfaced to a PDZ Europa 20–20 isotope ratio mass spectrometer (Sercon Ltd, Cheshire, UK). The final δ values (per mil, ‰), are expressed relative to international standards V-PDB (Vienna PeeDee Belemnite) carbon.

Material Movement Models

Surficial Material Movement from ***^{210}Pb*** – Analytical Model

Klaminder *et al.* (2014) developed an analytical solution for estimating the rate of surficial movement from radial transect points along an NSC using ^{210}Pb$_{ex}$ inventories. This model assumes piston-type flow of the soil matrix across the NSC surface, where ^{210}Pb$_{ex}$ is continuously deposited at the surface. Therefore, gains of ^{210}Pb$_{ex}$ to the soil matrix are atmospherically derived and losses are through radioactive decay. This mass balance can be described as:

$$\frac{dI}{d\ell} = \frac{D}{V_{surf}} - \frac{\lambda}{V_{surf}} I \tag{1}$$

where I is the total profile inventory ^{210}Pb$_{ex}$ (atoms m^{-2}), ℓ is the distance from the centre of the circle (m), D is the atmospheric deposition rate of ^{210}Pb$_{ex}$ (atoms m^{-2} year^{-1}), V_{surf} is the apparent piston flow velocity (m year^{-1}) and λ is the radionuclide decay constant (equal to $ln(2)/t_{1/2}$, with units of year^{-1}), where $t_{1/2}$ is the radionuclide half-life (years).

The atmospheric deposition rate of ^{210}Pb$_{ex}$ can be estimated by assuming steady-state inventories. Then, D (atoms m^{-2} year^{-1}) is equal to the annual amount of inventory loss by decay. Therefore, at steady state:

$$D = \frac{I_{ss} - I_{ss} e^{-\lambda t}}{t} \tag{2}$$

where D is the atmospheric deposition rate of ^{210}Pb$_{ex}$ (atoms m^{-2} year^{-1}), I_{ss} is the chosen steady-state reference inventory of ^{210}Pb$_{ex}$ (atoms m^{-2}) and t is the time period under consideration (years), generally evaluated at $t = 1$.

Where significant physical movement of material occurs relative to the half-life of ^{210}Pb$_{ex}$, as in NSCs, estimates of I_{ss} (atoms m^{-2}) cannot rely on a single point or profile inventory. Like Klaminder *et al.* (2014), we utilised the weighted area average inventory for all profiles (including both inner and outer domain), assuming a circular NSC and outer domain increments.

Rearranging Equation (1) we can infer surficial flow velocities between any two points with known inventories along the radial transect:

$$V_{surf} = \frac{(D - \lambda I)}{dI/d\ell} \tag{3}$$

Surficial Movement from short-Lived Radionuclide Tracers – Numerical Model

For pulse-like tracers (non-continuous fallout, such as ^{137}Cs (Appendix S1)), a steady-state condition cannot be assumed, and so developing analytical mass balance models is challenging. Therefore, numerical modelling is required to yield apparent movement rates. In our numerical model, the NSC inner domain is assumed to be circular and is

discretised into L increments. The numerical model is run for annual time steps where material is assumed to move radially outward as plug flow so that:

$$I_{\ell+\Delta\ell(t+\Delta t)} = \left(I_{\ell(t)} + D\Delta t\right)e^{-\lambda\Delta t}\ell + \Delta\ell \quad (4)$$

where $I_{\ell+\Delta\ell(t+\Delta t)}$ is the inventory (atoms m^{-2}) of the radial increment terminating at radial length $\ell+\Delta\ell$ in the next time step, $\Delta\ell = \Delta t V_{surf}$, where V_{surf} is the velocity of plug flow ($V_{surf} = \frac{\Delta\ell}{\Delta t}$), and D and λ are as defined in Equation 1. Because the upward-moving subsoil in the centre of the NSC has not been exposed to the atmospheric deposition of short-lived radionuclides, we set boundary conditions so that there is no $^{210}Pb_{ex}$ or ^{137}Cs activity at $\ell = 0$. Additionally, because material does not move on the surface beyond the edge of the inner domain (at the MT or mixing transition sampling point in our study), we assume that $v = 0$ at $\ell = L$, so the outermost increment collects the cumulative inventory of material moving into it, with loss only by radioactive decay.

Models are then run until the time since assumed pulse deposition is reached (^{137}Cs) or until steady-state is achieved (for $^{210}Pb_{ex}$ ~ 300–1000 years, depending on D). For ^{137}Cs, we assume pulse deposition in 1963 (Appendix S1). This does not account for any deposition from the Chernobyl incident, which did have a minimal influence on radionuclide inventories in Arctic Sweden (Barrie *et al.,* 1992). Therefore, our estimates of surficial movement via the ^{137}Cs tracer should be considered minimum velocity estimates. For ^{137}Cs, the $t = 0$ inventories are calculated from observed inventories in the outer domain (OD1 and OD2), which is assumed to reflect inventories in the absence of the physical movement of soil materials:

$$I_{\ell(t=0)} = \frac{I_{OD,ave}}{e^{-\lambda\left(t_{samp}-1963\right)}} \text{ for } ^{137}Cs \quad (5)$$

where $I_{OD,ave}$ is the average ^{137}Cs (atoms m^{-2}) inventory of the outer domain profiles (OD1 and OD2), and t_{samp} is the year (AD) of sampling. For ^{210}Pb, the $^{210}Pb_{ex}$ inventory at $t = 0$ is assumed to be zero, as inventories of $^{210}Pb_{ex}$ across the NSC are assumed to be developed on transported glacial sediments that have been ice-shielded before deglaciation, with no atmospherically derived ^{210}Pb ($^{210}Pb_{ex}$) inventories.

Upon completion of a numerical model run, 10-cm segments of the NSC (starting with the outermost portion) were summed to generate total expected radionuclide inventories (and subsequently activity inventories per unit ground area) for specific values of v (cm $year^{-1}$). The predictions for the numerical model (apparent rates) were taken as the best estimate and range of results from numerical runs that lay inside of the reported 1-sigma uncertainty in the observed inventories at each point.

Subsurface Movement from ^{14}C

To estimate subsurface rates of material movement, the range of 2-sigma uncertainties on apparent radiocarbon ages (cal years BP) derived from $\Delta^{14}C$ of bulk SOC was taken to represent the time since subduction of a cryoturbated parcel, an extension of the approach by Dyke and Zoltai (1980). A straight-line path was drawn from the previous marker of material movement (minimum path length) and along the sides of a right-angled triangle (maximum path length) between the two points. The apparent subsurface movement rate is then:

$$V_{sub} = \frac{p}{Y_2 - Y_1} \quad (6)$$

where V_{sub} is the movement velocity (cm $year^{-1}$), Y_1 is the apparent radiocarbon age of bulk SOC at the point of origin, Y_2 is the apparent radiocarbon age of bulk SOC at the end point and p is the path length (cm).

For paths beginning with an origin at or near the surface (i.e. the initial subduction of material from the mixing transition (MT) or the edge of the outer domain – the hypothesised origin of subducted organic material in the equilibrium cell model) – we bracket a range of possible initial radiocarbon ages (before subduction or subsurface movement) as follows. (i) Initial age minimum: the minimum initial radiocarbon age of cryoturbated material – represented by surficial bulk SOC between MT and OD1 – can be assumed to be 0 (modern C at the time of subduction). (ii) Initial age maximum: we constrain the maximum initial age of cryoturbated material using ^{14}C profiles from a similar NSC at the same study site, described in Klaminder *et al.* (2014), where the maximum age of organic materials (extending to 11 cm depth) from the outer domain was estimated at 200 ± 100 years. We add 100 years to this estimate (2-sigma maximum bracket) and arrive at our maximum initial radiocarbon age estimate of cryoturbated materials as 400 years at the time of subduction.

Surface Exposure Histories of Cryoturbated Materials

Meteoric ^{10}Be and Hgin excess of geogenic or inherited concentrations can provide novel estimates of the surface exposure histories (i.e. the amount of time spent exposed to atmospheric deposition at or near the soil surface) for cryoturbated parcels when atmospheric deposition rates are constrained. We utilise three different long-term atmospheric deposition rates for ^{10}Be in this study: 0.8×10^{10} atoms m^{-2} $year^{-1}$ (Willenbring and von Blanckenburg, 2010), 0.35×10^{10} atoms m^{-2} $year^{-1}$ (Finkel and Nishiizumi, 1997), and the D_{atm} derived from the equation below, when t is constrained by deglaciation chronologies of approximately 9000 years near Abisko (Lundqvist, 2004):

$$\frac{D_{atm} = I_{10}Be, ave}{t_{glac}} \quad (7)$$

where D_{atm} is the long-term average deposition rate of meteoric ^{10}Be (atoms m^{-2} $year^{-1}$), $I_{10Be,ave}$ is the average

^{10}Be inventory across all profiles (atoms m^{-2}) and t_{glac} is the time since deglaciation (years). For Hg, we utilised three different deposition rates: 2×10^{-6} ng m^{-2} year^{-1}, the average of 1999–2002 Hg wet deposition at a station in Pallas, Finland, latitude 67°58′N (Munthe *et al.,* 2007), 1×10^{-6} ng m^{-2} year^{-1} and 5×10^{-7} ng m^{-2} year^{-1}, representing a range of estimated pre-industrial Hg deposition rates in south-central Sweden (Bindler, 2003).

The maximum surficial exposure history (time spent exposed to atmospheric deposition at or near the soil surface of a subducted parcel) is equal to the inventory of excess ^{10}Be or Hg in a soil parcel or profile section divided by the atmospheric deposition rate:

$$t_{res} = \frac{I_{excess,n}}{D_{atm}} \quad (8)$$

where t_{res} is the surficial residence time (the cumulative time of atmospheric exposure (years)), $I_{excess,n}$ is the excess ^{10}Be (atoms m^{-2}) or Hg (mg m^{-2}) inventory – defined below – (atoms m^{-2}) of a cryoturbated parcel n, and D_{atm} is the atmospheric deposition rate (atoms m^{-2} year^{-1}). For the purposes of this model, excess ^{10}Be or Hg (Hg_{ex}) inventories of cryoturbated parcels were calculated as the difference between the inventory of the increment under consideration and the next higher depth increment.

RESULTS

Morphological Aspects of Sampled Profiles

Sampling locations in the mineral centre (CM, 0 cm), inner domain (IN, 83 cm), mixing transition (MT, 145 cm) and outer domains (OD1 and OD2, 180 and 260 cm, respectively) showed distinct profile morphologies (Figure 2). Sampling locations CM and IN had no surficial organic horizon (0 cm depth), while profiles at MT, OD1 and OD2 had surficial organic horizons with thicknesses of 4, 6 and 8 cm, respectively (Figure 2). Additionally, profile IN had a morphologically distinct organic-rich layer at a depth of 36–42 cm (Figure 2). The elevation gradient between CM and OD2 was measured as 14 cm in the summer and 21 cm in the winter (a seasonal difference of 7 cm), which is evidence of ongoing differential frost-heave and reinforces current observations of activity in these NSCs (Figure 2).

Sample Characterisation, Elemental Concentrations and Radioisotope Activities

Trends in surficial pH across the NSC transect closely followed those of O horizon morphology and SOC concentration. A trend of decreasing surficial (uppermost sampling increment) pH from 5.4 to 3.6 occurred from CM to OD2. Inner domain samples were characterised by pH values greater than 5.0. Deep mineral soil increments had values of pH 5.2–5.4, while organic materials on the surface at MT, OD1 and OD2 were characterised by an average pH of 3.6.

SOC concentrations ranged from 0.2 to 41.8 per cent across all samples, and for the surficial depth increments increased across the radial transect associated with the change from mineral materials to organic materials from IN to MT. Average SOC concentrations for mineral depth increments (n = 35) were 1.6 ± 2.6 g 100 g^{-1} soil, while average SOC concentrations for surficial organic materials (from MT, OD1 and OD2; n = 3) were 39.0 ± 3.4 g 100 g^{-1} soil. SOC concentrations decreased with depth except for a morphologically distinct organic-rich layer at a depth of 36–42 cm in the IN profile (Figures 2 and 3) and an increase in SOC at the 22–32 cm depth increment in the CM profile (Table 1, Figure 3).

Total Hg spanned four orders of magnitude across all sampling increments (0.1–358 ng g^{-1}), and showed pronounced differences in surficial concentrations across the radial transect, consistent with observed trends of organic-layer thickness and SOC content. Geogenic concentrations of Hg, calculated as the average of the Hg concentration of the bottom depth increment for each profile, were estimated at 4.4 ± 0.8 ng g^{-1}. Averages of Hg_{ex} for organic and mineral sampling increments were 257 ± 90 and 10 ± 22 ng g^{-1}, respectively (Table 1).

δ^{13}C values averaged −25.9 ± 0.7 per mil across all sampling increments, with averages of −27.2 ± 0.5 per mil for organic materials and −25.7 ± 0.6 per mil for mineral sampling increments (Table 1). There were no apparent radial trends in profile-averaged δ^{13}C maximum, minimum or mean values. However, δ^{13}C values of SOC generally became more enriched (less negative) in all profiles with depth, with the exception of the same two increments (IN 36–42 and CM 22–32) that showed relative SOC enrichment with depth. δ^{13}C values were negatively correlated with bulk SOC (more negative or less enriched with increasing SOC) across all depth increments (R^2 = 0.44, $p < 0.0001$, Figure 3). Further analysis of the relationship between bulk SOC and δ^{13}C is provided in the Supporting information (Appendix S1, Figure S3).

Activities of $^{210}Pb_{ex}$ across all depth increments ranged from 0 (below detection limit) to 311 Bq kg^{-1}, and except for a decline within analytical error from CM to IN, showed increasing trends from 38 to 311 Bq kg^{-1} for surficial sampling increments across the NSC radial transect. In all cases, the surficial depth increment had the highest activity of $^{210}Pb_{ex}$ (Table 1, Figure 3). ^{137}Cs activities ranged from 0 to 108 Bq kg^{-1} across all sampling increments and in contrast to $^{210}Pb_{ex}$ did not always have the highest activities in the surficial depth increment of each profile (Table 1, Figure 3). For profiles MT and OD2, the highest ^{137}Cs activities were measured in the 4–7 and 8–15 cm depth increments, respectively. Despite this, the profile of maximum ^{137}Cs activity increased in an outward direction along the radial transect. Therefore, $^{210}Pb_{ex}$ was consistently detected in the top 15–20 cm of all profiles (Table 1), while the depth of ^{137}Cs detection varied significantly. No ^{137}Cs was detected at location CM, while

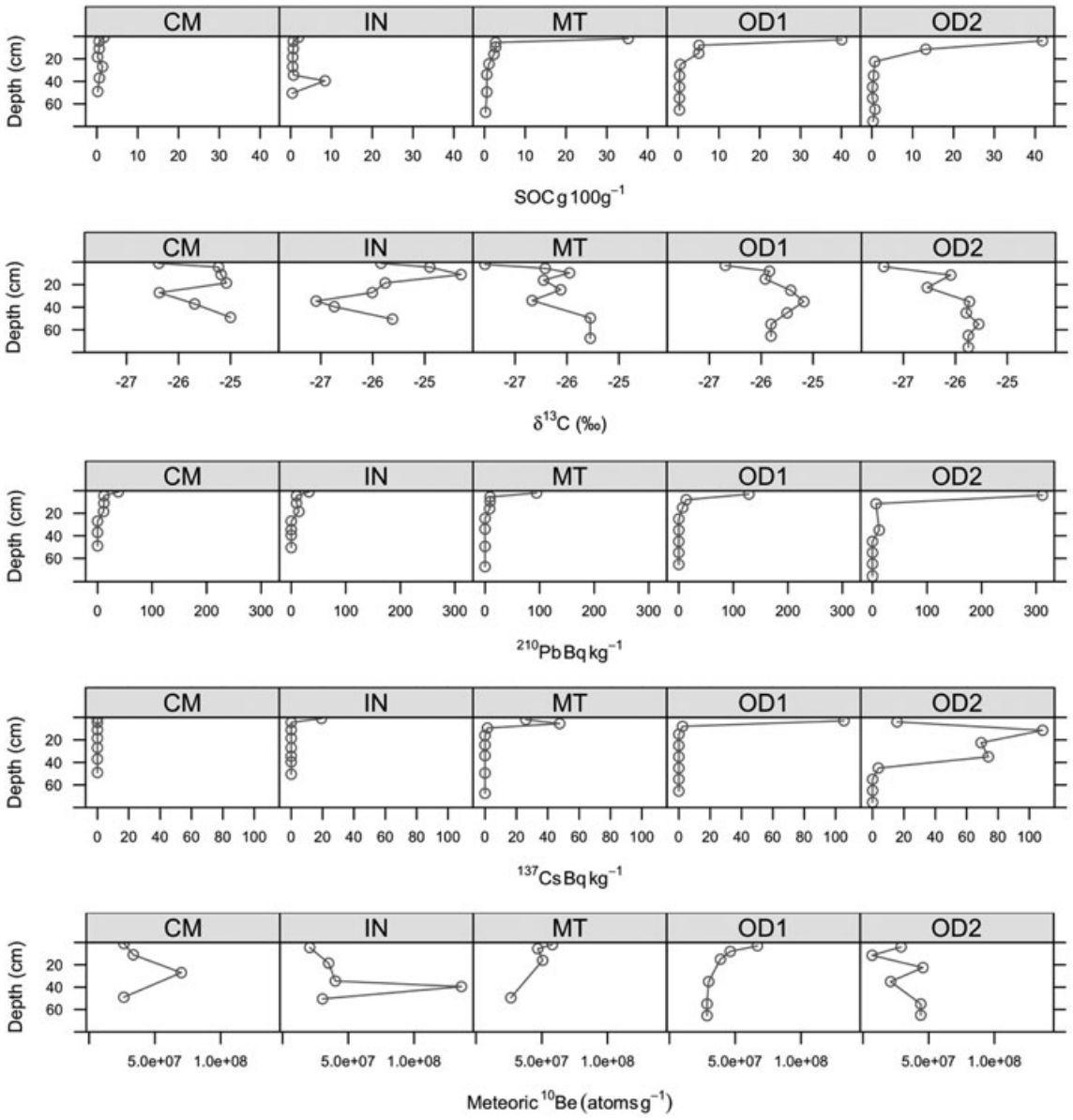

Figure 3 Profile depth distributions for soil organic carbon (SOC), $\delta^{13}C$, ^{210}Pb, ^{137}Cs and meteoric ^{10}Be.

^{137}Cs was detected to depths of 2, 12, 10 and 50 cm at locations IN, MT, OD1 and OD2, respectively (Table 1).

Profile integrated inventories of $^{210}Pb_{ex}$ and ^{137}Cs varied across the radial transect (Appendix S1, Table S4, Figure S4). Weighted, area-normalised inventories of $^{210}Pb_{ex}$ (including both inner and outer domain sampling locations, approximating steady-state) were 3307 ± 281 Bq m^{-2} (Appendix S1), resulting in a long-term average $^{210}Pb_{ex}$ deposition rate of 101 ± 14 Bq m^{-2} (Equation 2). Original (AD 1963) ^{137}Cs inventories from pulse deposition were estimated at 4306 ± 508 Bq m^{-2} (Equation 5). Further analysis of the relationships between the radioisotope tracers utilised in this study as well as the variability in their area-normalised inventories is provided in the Supporting Information (Appendix S1, Table S4; Figures S2 and S4).

^{10}Be concentrations averaged 4.12 ± 2.45 × 10^7 atoms g^{-1} across all sampling increments (with averages of 3.98 ± 2.52 × 10^7 and 5.13 ± 1.98 × 10^7 atoms g^{-1} for mineral and organic materials, respectively) with a total range from 0.7 to 13.6 × 10^7 atoms g^{-1} (Figure 3). Profile trends of meteoric ^{10}Be showed striking variability in shape and magnitude across the radial transect, with significant subsurface peaks at locations CM and IN, generally declining trends with depth at MT and OD1, and a slightly increasing trend with depth at OD2 (Figure 3). Estimates of meteoric ^{10}Be inheritance in the till parent material (calculated from the average of the bottom depth increments for each sampling point) resulted in 2.85 ± 0.20 × 10^7 atoms g^{-1}.

The cryoturbated parcel at 37–42 cm depth increment at sampling location IN had an SOC content of 8.4 ± 0.9 g

Table 1 Tracer concentrations and activities across radial non-sorted circle transect sampling profiles.

Location	Depth (cm)	SOC (%)	Hg_{ex} (ng g^{-1})	$\delta^{13}C$ (‰)	^{137}Cs (Bq kg^{-1})	$^{210}Pb_{ex}$ (Bq kg^{-1})	^{10}Be (10^7 atoms g^{-1})
Center (CM)	0–2	1.7 ± 0.19	24 ± 0.9	−26.4 ± 0.20	0	38 ± 5.7	2.65 ± 0.09
	2–7	0.6 ± 0.06	24 ± 0.9	−25.2 ± 0.19	0	12 ± 1.7	—[1]
	7–15	0.6 ± 0.06	0 ± 0	−25.2 ± 0.19	0	12 ± 1.7	3.36 ± 0.11
	15–22	0.2 ± 0.02	0.94 ± 0.03	−25.1 ± 0.19	0	0	—
	22–32[2]	1.4 ± 0.15	6.8 ± 0.3	−26.4 ± 0.20	0	0	7.01 ± 0.21
	32–42	0.6 ± 0.07	0 ± 0	−25.7 ± 0.20	0	0	—
	42–56	0.2 ± 0.02	0.03 ± 0.01	−25.0 ± 0.19	0	0	2.64 ± 0.08
Inner (IN)	0–2	1.9 ± 0.21	15 ± 0.6	−25.8 ± 0.20	19 ± 1.1	33 ± 4.9	—
	2–7	0.6 ± 0.07	1.37 ± 0.05	−24.9 ± 0.19	0	10 ± 1.4	2.07 ± 0.05
	7–15	0.6 ± 0.07	1.37 ± 0.05	−24.3 ± 0.19	0	10 ± 1.4	—
	15–22	0.5 ± 0.06	0 ± 0	−25.8 ± 0.20	0	14 ± 2.1	3.51 ± 0.08
	22–32	0.5 ± 0.06	4.9 ± 0.2	−26.0 ± 0.20	0	0	—
	32–37	0.7 ± 0.08	12.6 ± 0.5	−27.1 ± 0.20	0	0	4.01 ± 0.14
	37–42[3]	8.4 ± 0.93	56 ± 2	−26.7 ± 0.21	0	0	13.6 ± 0.17
	42–59	0.4 ± 0.04	2 ± 0.08	−25.6 ± 0.20	0	0	3.04 ± 0.09
Mixing transition (MT)	0–4	35.2 ± 3.91	176 ± 7	−27.6 ± 0.21	26 ± 1.5	94 ± 14	5.80 ± 0.18
	4–7	2.7 ± 0.30	20.4 ± 0.8	−26.4 ± 0.20	48 ± 3.1	9 ± 1.4	4.69 ± 0.14
	7–12	2.7 ± 0.30	20.4 ± 0.8	−26.0 ± 0.20	1.5 ± 1.0	9 ± 1.4	—
	12–20	2.3 ± 0.26	6.9 ± 0.3	−26.5 ± 0.20	0	8 ± 1.3	5.07 ± 0.16
	20–29	1.1 ± 0.12	3.1 ± 0.1	−26.1 ± 0.20	0	0	—
	29–39	0.6 ± 0.07	5.3 ± 0.2	−26.7 ± 0.21	0	0	—
	39–60	0.6 ± 0.07	5.3 ± 0.2	−25.6 ± 0.20	0	0	2.65 ± 0.08
	60–71	0.3 ± 0.03	0.70 ± 0.03	−25.6 ± 0.20	0	0	—
Outer domain 1 (OD1)	0–6	40.1 ± 4.44	240 ± 9	−26.7 ± 0.21	105 ± 4.8	128 ± 19	6.69 ± 0.16
	6–10	5.1 ± 0.57	54 ± 2	−25.9 ± 0.20	2 ± 0.7	14 ± 2	4.62 ± 0.13
	10–20	5.0 ± 0.56	3.1 ± 0.1	−25.9 ± 0.20	0	7 ± 1	3.88 ± 0.08
	20–30	0.5 ± 0.06	1.67 ± 0.06	−25.9 ± 0.20	0	0	—
	30–40	0.3 ± 0.04	0.13 ± 0.01	−25.2 ± 0.19	0	0	2.98 ± 0.11
	40–50	0.3 ± 0.04	0.33 ± 0.01	−25.5 ± 0.20	0	0	—
	50–71	0.3 ± 0.03	0.04 ± 0.01	−25.8 ± 0.20	0	0	2.86 ± 0.07
Outer domain 2 (OD2)	0–8	41.8 ± 4.63	355 ± 14	−27.4 ± 0.21	16 ± 4.5	311 ± 47	2.90 ± 0.09
	8–15	13.2 ± 1.46	112 ± 4	−26.1 ± 0.20	108 ± 6.3	6 ± 1	0.70 ± 0.02
	15–30	0.7 ± 0.07	11.2 ± 0.4	−26.5 ± 0.20	69 ± 5.0	0	4.56 ± 0.09
	30–40	0.4 ± 0.05	2.7 ± 0.1	−25.7 ± 0.20	74 ± 2.5	0	2.10 ± 0.05
	40–50	0.2 ± 0.02	0 ± 0	−25.8 ± 0.20	4 ± 1	0	—
	50–60	0.2 ± 0.02	0 ± 0	−25.6 ± 0.20	0	0	4.39 ± 0.11
	60–70	0.8 ± 0.08	0.67 ± 0.02	−25.6 ± 0.20	0	0	4.39 ± 0.11
	70–81	0.3 ± 0.03	0.33 ± 0.01	−25.6 ± 0.20	0	0	—

[1]—, Not Determined.
[2]Cryoturbated parcel; $\Delta^{14}C = -258 \pm 3$ per mil, conventional ^{14}C age ($\delta^{13}C$ corrected) = 2400 ± 30 BP, range of 2σ calibrated age = 2350–2680 cal years BP.
[3]Cryoturbated parcel; $\Delta^{14}C = -202 \pm 4$‰, conventional ^{14}C age ($\delta^{13}C$ corrected) = 1960 ± 30 BP, range of 2σ calibrated age = 1860–1990 cal years BP.

100 g^{-1}, a bulk SOC $\Delta^{14}C$ of −202 ± 4 per mil and a 2-sigma uncertainty range in radiocarbon age of 1860–1990 cal years BP. The 22–32 cm depth increment at sampling location CM had an SOC content of 1.4 ± 0.2 g 100 g^{-1}, a bulk SOC $\Delta^{14}C$ of −258 ± 3 per mil and 2-sigma uncertainty in radiocarbon age of 2350–2680 cal years BP.

Material Movement Rate Estimates

Input data used for the modelling of apparent movement rates are shown in Table 2. Apparent soil movement rates differed between domain sections and between the surface and subsurface. Apparent rates of surficial movement were 2.6 and 0 cm $year^{-1}$ for the analytical solution $^{210}Pb_{ex}$ model between CM-IN and IN-MT, respectively, for an inner domain numerical rate average of 1.3 cm $year^{-1}$ (Table 2). Numerical models for $^{210}Pb_{ex}$ resulted in apparent rates of 0–1.0 cm $year^{-1}$ for the CM-IN and 0–0.1 for the IN-MT increments, with an inner domain average of 0.22 cm $year^{-1}$ (Table 2). Calculating averages for both analytical and numerical models with ^{137}Cs and ^{210}Pb observations resulted in an apparent average rate across the inner domain of 0.76 cm $year^{-1}$ (Table 2). Averages of numerical models applied to observed ^{137}Cs inventories were 1.2 and 0.1 cm $year^{-1}$ for CM-IN and IN-MT increments, respectively, for an entire inner domain average of

Table 2 Apparent movement rates derived from various tracers, models and locations across the non-sorted circle. The results of numerical models for ^{137}Cs, $^{210}Pb_{ex}$ and ^{14}C analytical models are reported as ranges of all results (minimum–maximum). The results of analytical models for $^{210}Pb_{ex}$, ^{10}Be and Hg are reported as standard deviations (1-sigma uncertainties) from propagated errors.

$^{210}Pb_{ex}$: surficial movement					
Model	Location	Fallout rate (D_{atm}) (Bq m^{-2} year^{-1})		Inventory difference (Bq m^{-2})	Apparent rate (cm year^{-1})
Analytical	CM to IN	101 ± 14		659 ± 559	2.55 ± 0.4
	IN to MT	101 ± 14		763 ± 740	0 ± 2.6
Numerical	CM to IN	101 ± 14		659 ± 559	0–1.0
	IN to MT	101 ± 14		763 ± 740	0–0.1
^{137}Cs: surficial movement					
Model	Location	Original inventory (Bq m^{-2})		Inventory difference (Bq m^{-2})	Apparent rate (cm year^{-1})
Numerical	CM to IN	4306 ± 508		405 ± 65	1.1–1.3
	IN to MT	4306 ± 508		1334 ± 328	0–0.2
^{14}C: subduction and Subsurface movement					
Model	Location	Initial age (years)[1]	Path length (cm)	Age difference (95% CI (years))	Apparent rate (cm year^{-1})
Linear minimum path	MT to IN	0	88	1860–1990	0.04–0.05
	MT to IN	400	88	1460–1590	0.06–0.06
	IN to CM	n/a[b]	84	360–820	0.10–0.23
Linear maximum path	MT to IN	0	117	1860–1990	0.06–0.06
	MT to IN	400	117	1460–1590	0.07–0.08
	IN to CM	n/a	96	360–820	0.12–0.27
^{10}Be: maximum surface exposure histories of cryoturbated parcels					
Model	Location	Deposition rate (10^6 atoms cm^{-2} year^{-1})		Parcel inventory $^{10}Be_{ex}$ (atoms cm^{-2})	Maximum exposure (years)
Atmospheric accumulation	IN 38–42 cm	0.8 (Ebert *et al.,* 2012)		3.4 ± 0.7 × 10^8	425 ± 87
		0.35 (Finkel and Nishiizumi, 1997)		3.4 ± 0.7 × 10^8	971 ± 200
		0.2 (this study)		3.4 ± 0.7 × 10^8	1700 ± 350
	CM 22–32 cm	0.8 (Ebert *et al.,* 2012)		2.5 ± 0.8 × 10^8	313 ± 100
		0.35 (Finkel and Nishiizumi, 1997)		2.5 ± 0.8 × 10^8	714 ± 229
		0.2 (this study)		2.5 ± 0.8 × 10^8	1250 ± 400
Hg: maximum surface exposure histories of cryoturbated parcels					
Model	Location	Deposition rate (mg m^{-2} year^{-1})		Parcel inventory Hg_{ex} (mg m^{-2})	Maximum exposure (years)
Atmospheric accumulation	IN 38–42 cm	0.002 (Munthe *et al.,* 2007)		1.97 ± 0.30	986 ± 148
		0.001 (Bindler, 2003)		1.97 ± 0.30	1970 ± 296
		0.0005 (Bindler, 2003)		1.97 ± 0.30	3940 ± 591
	CM 22–32 cm	0.002 (Munthe *et al.,* 2007)		0.48 ± 0.07	238 ± 35
		0.001 (Bindler, 2003)		0.48 ± 0.07	476 ± 71
		0.0005 (Bindler, 2003)		0.48 ± 0.07	952 ± 143

[1]Initial age constraints on cryoturbated parcels are relevant only for the MT to IN path; the minimum initial age is 0 (modern at the time of subduction), while the maximum initial age is constrained at 400 years using data from Klaminder *et al.* (2014) as described in Materials and Methods.
[2]n/a, not applicable. Initial age constraints not relevant for the IN to CM path as cryoturbated parcel age is constrained at IN.

0.65 cm year^{-1}. Overall rate averages for both ^{137}Cs and $^{210}Pb_{ex}$ across all models were 1.4 cm year^{-1} for CM-IN, 0.05 cm year^{-1} for IN-MT and 0.7 cm year^{-1} across the whole inner domain (Table 2).

Apparent rates of subsurface movement derived from the radiocarbon age of bulk SOC in cryoturbated parcels were calculated based on assumptions of (i) continuous movement and (ii) linear minimum and maximum path lengths (with the assumed starting location between MT and OD1 (Figure 2, Table 2)). These resulted in rate averages of 0.06 cm year^{-1} for the MT-IN increment and 0.18 cm year^{-1} for the IN-CM increment (Table 2). Overall averages for all scenarios, increments and path lengths were 0.1 cm year^{-1} for subduction and subsurface movement (Table 2).

Estimates of the average of maximum exposure years for the two inner domain cryoturbated parcels based on excess ^{10}Be inventory are 1032 ± 640 years (average and standard deviation of results from all three deposition rates) for the cryoturbated parcel at IN 37–42 cm and 759 ± 470 years for the parcel at CM 22–32 cm, respectively. Similarly,

the maximum apparent surficial exposure years for all three deposition rates based on Hg_{ex} inventory are 2298 ± 1504 and 555 ± 363 years for IN 37–42 cm and CM 22–32 cm, respectively (Table 2).

DISCUSSION

Inferences from Meteoric ^{10}Be and ^{14}C

Our study is the first to examine the distribution and inventories of meteoric ^{10}Be across small-scale patterned-ground features such as NSCs. We are aware of no other study that has reported on densely investigated ^{10}Be profiles within small horizontal distances, and the variability between sampling locations in a small area reported here is striking. Meteoric ^{10}Be concentrations showed a spiked distribution with depth at sampling locations CM and IN, corresponding with cryoturbated parcels in the subsurface (Table 1, Figure 4). In contrast, decreasing distributions with depth were observed at locations MT and OD1, while increases with depth were observed at location OD2 (Table 1, Figure 4).

Two other studies have reported ^{10}Be concentrations in permafrost-affected soils, but no more than one profile at a single sampling site. In a non-glaciated region of northern Alaska, Bierman *et al.* (2014) observed a hump-like depth distribution that they attributed to leaching, as well as ^{10}Be concentrations one to two orders of magnitude higher than those reported here. Ebert *et al.* (2012) investigated ^{10}Be profiles in saprolite underlying glacial deposits in northern Sweden, and also found much higher concentrations of ^{10}Be. The ^{10}Be concentrations reported at our site are relatively low compared to these other studies because the NSC has developed in much younger (~9000 years old) till deposits.

No other studies have estimated the surface residence times of cryoturbated materials, but our analysis of ^{10}Be and Hg accumulation allowed us to provide primary, independent constraints on these time periods. The time periods estimated from these independent tracers are highly convergent for the parcel at CM 22–32 cm (313–1250 years (^{10}Be) and 238–952 years (Hg_{ex})), but the Hg_{ex} tracer results in approximately twofold longer estimates of surficial residence times at IN 37–42 cm (425–1700 (^{10}Be) and 986–3940 (Hg_{ex})). The large difference in excess ^{10}Be and Hg inventory in CM and IN parcels suggests a non-continuous or stochastic mechanism of subduction that is congruent with previous hypotheses related to cryoturbation mechanisms in NSCs and climatic triggers (Bockheim, 2007; Becher *et al.,* 2013).

The radiocarbon ages reported for subducted organic material in this study (1860–1990 and 2350–2680 cal years BP) are convergent with those from other subducted materials in NSCs on a global basis (Bockheim, 2007; Kaiser *et al.,* 2007; Becher *et al.,* 2013). In a study at the Abisko site, Becher *et al.* (2013) measured radiocarbon contents of 12 buried organic horizons in NSCs and found a range of radiocarbon ages from 0 to 1960 cal years BP. Bockheim (2007) compiled published ages from organic inclusions beneath patterned ground and found a range from 240 to 10 000 cal years BP. Both studies concluded that the ages of buried organic materials at least loosely coincided with periods of climatic warming, and hypothesised that under some scenarios modest warming may increase cryoturbation activity. The radiocarbon age of the cryoturbated parcel at CM (22–32 cm) in our study does roughly coincide with an inferred warming period near Abisko based on reconstructions of glacial advances (Becher *et al.,* 2013).

Convergent Markers for Determining Material Provenance and Surface History

The tracers most closely associated with the surficial exposure of soil materials in addition to ^{10}Be are SOC, Hg, $\delta^{13}C$, ^{137}Cs and $^{210}Pb_{ex}$. The facts that no ^{137}Cs or $^{210}Pb_{ex}$ was detected below 15 cm in the inner domain and that all profiles showed decreasing ($^{210}Pb_{ex}$) or shallow subsurface peaks (^{137}Cs) provide a primary constraint on soil movement in this NSC. That is, the subduction and subsurface movement of soil materials cannot be occurring at rates faster than decadal to century timescales (^{137}Cs and $^{210}Pb_{ex}$ half lives of 20–30 years). These patterns agree with previous studies in both the Alaskan and Swedish Arctic (Jelinski, 2013; Klaminder *et al.,* 2014), which found no detectable ^{137}Cs in the mineral materials at NSC centres and no deep subsurface ^{137}Cs or $^{210}Pb_{ex}$ activities, but significant near-surface inventories at the far edges of the inner domain and in the outer domain.

Two other studies have examined ^{210}Pb distributions and inventories with the intent to qualitatively or quantitatively estimate the rates and patterns of material movement in NSCs. Hagedorn *et al.* (2008) observed increasing ^{210}Pb activities with distance from an NSC centre, and Klaminder *et al.* (2014) used $^{210}Pb_{ex}$ to quantify rates of lateral soil movement along the NSC inner domain surface. In each study, ^{210}Pb activities and inventories increased with increasing distance from the NSC centre (CM) to the mixing transition (MT).

The whole-transect weighted average inventory of Hg_{ex} was 5.1 mg Hg m^{-2}, which is close to the range (5.6–7.8 mg Hg m^{-2}) of previously observed inventories in regional soils on a tundra peat hummock landscape (Klaminder *et al.,* 2008). Hg appears to be a conservative tracer of cryoturbated materials that were exposed to the surface even during pre-industrial ages, because natural Hg deposition rates (Bindler, 2003) are significant relative to the Hg contained in soil materials. However, it is important to note that recent depositional histories for Hg in southern Sweden also exhibit a peak at least one to two orders of magnitude higher than background rates in the 1950–70s followed by a decline over the following three decades (Bindler, 2003).

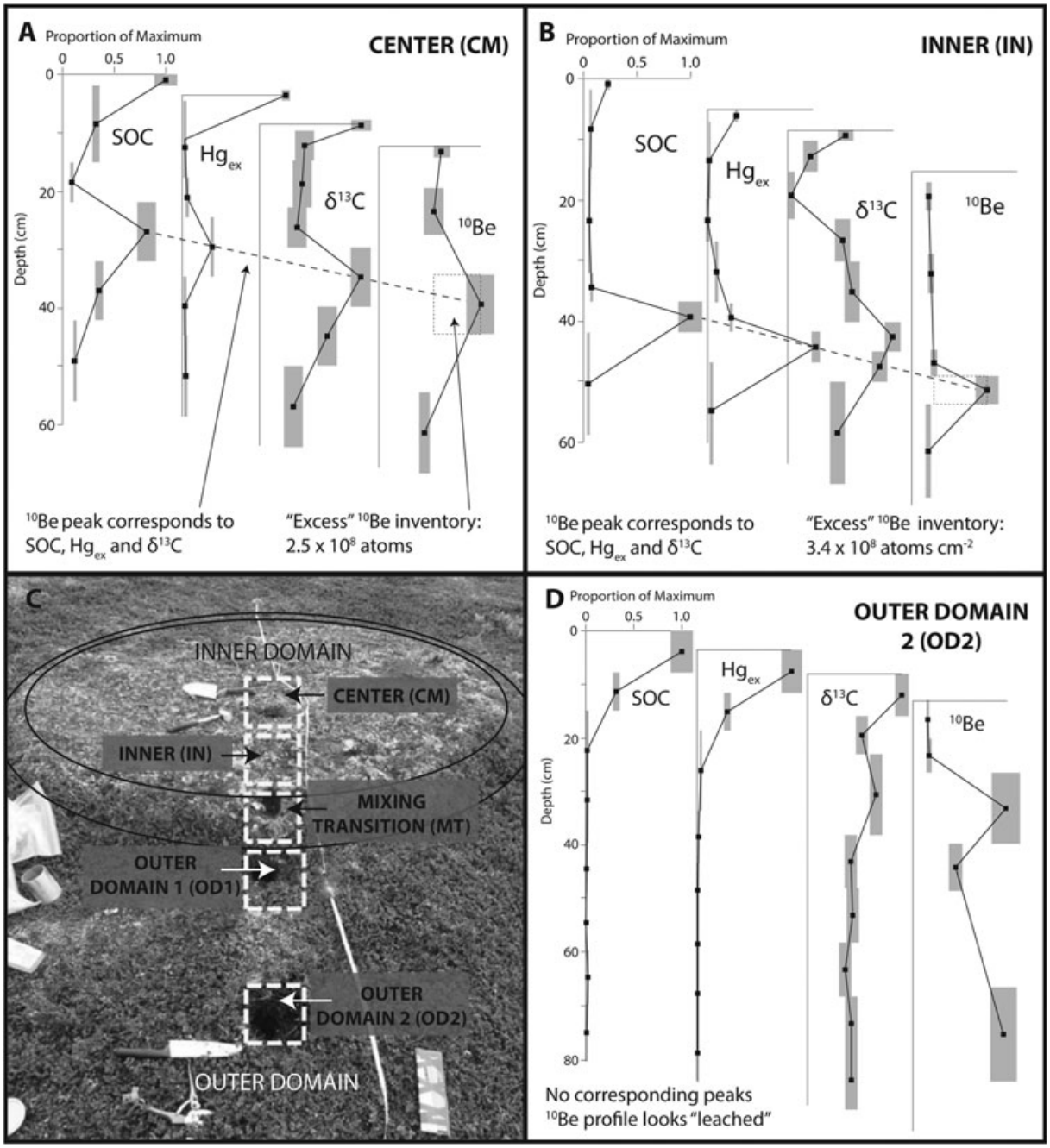

Figure 4 Normalised (to profile maximum) soil organic carbon (SOC), Hg_{ex}, $\delta^{13}C$ and meteoric ^{10}Be concentrations for selected profiles across the studied non-sorted circle. Centre (CM) and inner domain (IN) sampling points (panels a and B, respectively) show convergence of tracer peaks, indicating subducted material, while outer domain 2 (OD2 – panel D), shows no subsurface peak convergence and apparent leaching of ^{10}Be. Image in panel C is adapted from Makoto and Klaminder (2012).

If a material parcel has been buried for longer than ~100 years, ^{137}Cs and $^{210}Pb_{ex}$ will probably be below detectable limits, leaving SOC, Hg, $\delta^{13}C$ and ^{10}Be as the most conservative long-term tracers of surficial origin. Therefore, in evaluating sampling increments that are buried but show evidence of surficial origin, these four tracers should show convergent peaks in the subsurface (Figure 4 A and B). For example, our original sampling did not identify the parcel from 22 to 32 cm at CM as a cryoturbated parcel from morphology alone (SOC is only slightly elevated as compared to surrounding depth increments (1.4 and 0.6%, respectively) and similar to the relatively low surficial values at CM (1.7%)). The convergence of peaks in SOC, $\delta^{13}C$, Hg and ^{10}Be, however, clearly

establish the surficial origin of this sample (Figure 4) and allowed the prioritisation of ^{14}C analysis to estimate subsurface movement rates from IN to CM. In contrast, apparent peaks in any one or two of these tracers in outer domain profiles are not convergent, and may be attributed to leaching or differential retention processes (Figure 4D). Specifically, the depth functions of ^{210}Pb, ^{137}Cs, and ^{10}Be (Table 1, Figure 4) suggest that among our sampling locations across this particular NSC, the outer domain areas (OD1 and OD2) maintained a relatively stable status over the period of NSC development and function. In particular, the effects of leaching on ^{10}Be depth profiles (interpreted as subsurface increases in ^{10}Be but lack of convergence with SOC, Hg and $\delta^{13}C$) could be detected only at OD2, which is farthest from the inner domain.

Apparent Rates and Patterns of Material Movement

The estimates of material movement rate derived from radionuclide and elemental tracers in this study provide unique empirical insights into different aspects of material movement across multiple timescales in a single NSC. Previous work on the apparent rates of movement in NSCs has focused primarily on individual components of movement patterns, which we compile here to place our estimated rates in context. Specifically, we examine previously estimated rates of centre upward movement (Figure 1, arrow 1), lateral surficial movement (Figure 1, arrow 2), and subduction and subsurface movement (Figure 1, arrow 3) in NSCs and related patterned ground (Table 3).

Centre upward movement due to ice-lens formation and heave (Figure 1, arrow 1) is not directly quantified in our work, but previous studies have estimated net upward material movement in the NSC centre from 0 to 1.5 cm year^{-1} (Table 3). Because the extent and magnitude of differential frost heave (Peterson and Krantz, 2003) drives the net upward motion in individual NSCs, and is highly dependent on many environmental factors such as vegetation, hydrological conditions and parent material (Daanen *et al.,* 2008), we expect that these rates vary significantly between sites. Nonetheless, rates derived from physical and short-lived radioisotope tracers and across NSCs from Canada and Sweden are convergent in magnitude (Table 3).

Lateral surficial movement (Figure 1, arrow 2) has been the most extensively studied and quantified form of material movement in NSCs because it is easier to observe and measure than subsurface movement. Surficial movement rates derived from photogrammetry of sorted circles (Kääb *et al.,* 2013), and physical tags (Egginton and Shilts, 1978; Sawyer, 2007) and $^{210}Pb_{ex}$ (Klaminder *et al.,* 2014) in NSCs have resulted in similar magnitudes of lateral movement rate estimates of 0–4.5 cm year^{-1} (Table 3), across NSCs in different environments (USA, Canada, Norway and Sweden, annual average temperatures of −11 to −2°C and annual average precipitation of 270–848 mm). If rate estimates are divided into subsections of the NSC inner domain, lateral movement rates nearest to the centre of the NSC are typically two to five times greater than those rates in the outer portions of the inner domain. The use of both analytical and numerical models for ^{137}Cs and ^{210}Pb for the NSC in our study resulted in similar inferred magnitudes and patterns of lateral movement rates. Rates in our NSC derived from $^{210}Pb_{ex}$ and ^{137}Cs for the proximal part of the inner domain (CM-IN) ranged from 0 to 2.6 cm year^{-1}, while rates for the distal portion of the inner domain (IN-MT) ranged from 0 to 0.2 cm year^{-1} (Table 2).

Subduction and subsurface movement rates (Figure 1, arrow 3) have previously been estimated primarily by

Table 3 Compilation of published material movement rate estimates in non-sorted and sorted (Hallet *et al.,* 1988; Kääb *et al.,* 2013) circles for four movement types using different tracers, including this study.

Movement type	Method	Apparent rates	Location	Reference
Centre Upward (Figure 1, arrow 1[1])	^{210}Pb	0.2–0.7 cm year^{-1}	Abisko, Sweden	Klaminder *et al.* (2014)
	Telescopic probes	0.4–1.2 cm year^{-1}	Alberta, Canada	Harris (1998)
	Tube intrusion	0–1.5 cm year^{-1}	Nunavut, Canada	Egginton and Shilts (1978)
Surficial lateral movement (Figure 1, arrow 2)	Photogrammetry	0.3–2.0 cm year^{-1}	Svalbard, Norway	Kääb *et al.* (2013)
	Physical markers	<1.0–3.0 cm year^{-1}	Montana, USA	Sawyer (2007)
	Physical markers	0–3.8 cm year^{-1}	Nunavut, Canada	Egginton and Shilts (1978)
	Physical markers	~1 cm year^{-1}	Spitsbergen, Norway	Hallet *et al.* (1988)
	^{210}Pb	3.1–4.5 cm year^{-1}	Abisko, Sweden	Klaminder *et al.* (2014)
	^{137}Cs	0–1.3 cm year^{-1}	Abisko, Sweden	This study
	^{210}Pb	0–2.55 cm year^{-1}	Abisko, Sweden	This study
Subduction/subsurface movement (Figure 1, arrow 3)	$^{210}Pb - {}^{14}C$	0.01–0.012 cm year^{-1}	Abisko, Sweden	Becher *et al.* (2013)
	^{14}C	0.03–0.1 cm year^{-1}	Nunavut, Canada	Dyke and Zoltai (1980)
	^{14}C	0.02–0.05 cm year^{-1}	Spitsbergen, Norway	Hallet *et al.* (1988)
	^{210}Pb	0.3–1.2 cm year^{-1}	Abisko, Sweden	Klaminder *et al.* (2014)
	Telescopic probes	0.8–1.2 cm year^{-1}	Alberta, Canada	Harris (1998)
	^{14}C	0.04–0.27 cm year^{-1}	Abisko, Sweden	This study
Surface exposure history: cryoturbated parcels	^{10}Be	313–1700 years	Abisko, Sweden	This study
	Hg_{ex}	238–3940 years	Abisko, Sweden	This study

[1]Numbers refer to idealised movement patterns generalised in Figure 1.

$^{210}Pb_{ex}$ (Becher *et al.,* 2013; Klaminder *et al.,* 2014), ^{14}C (Dyke and Zoltai, 1980; Becher *et al.,* 2013) and telescopic probes (Harris, 1998; Table 3). These derived rates of subduction and subsurface movement average an order of magnitude lower than apparent rates of lateral movement (Table 3). In this study, we examined two cryoturbated parcels (representing two time points) with evidence of previous surficial origins (CM 22–32 cm and IN 36–42 cm). The difference in ^{14}C age between them allows us to place first-order constraints on the movement rate of subducted materials in the subsurface along the path of hypothesised movement, which appears to be an order of magnitude lower than apparent rates of surficial movement in the NSC (Table 2), consistent with previous studies (Table 3). Our data appear to suggest that the rates of subsurface movement may be faster nearer to the centre of the NSC, as apparent rates from the MT/OD1 surface or subsurface origin to 37–42 cm at IN were estimated at 0.04–0.08 cm $year^{-1}$, while apparent subsurface movement rates from IN to CM range from 0.10 to 0.27 cm $year^{-1}$.

There has been significant previous work on the measurement and modelling of seasonal frost-heave magnitude in NSCs (i.e. Peterson and Krantz, 2003; Romanovsky *et al.,* 2008; Klaus *et al.,* 2013), but fewer empirical observations of apparent material movement rates over periods longer than a year. Frost-heave and diapirism are most significant near the centre of NSCs and are the major processes driving cryoturbation in them (Shilts, 1978; Mackay, 1980; Swanson *et al.,* 1999; Peterson and Krantz, 2003; Nicolsky *et al.,* 2008). Studies using ^{210}Pb, telescopic probes and tube intrusion measurements have demonstrated 0–1.5 cm $year^{-1}$ of upward material displacement in the area where ice-lens growth is strongest (Table 3; Egginton and Shilts, 1978; Harris, 1998; Klaminder *et al.,* 2014). This may explain our observation that apparent rates of both surface and subsurface movement derived from our isotope suite at the centre of the NSC appear to be highest there, whereas the lateral flux and subduction process at the NSC edge appears to be slower (Table 2). The apparent differences in apparent velocities derived here may be caused by different mechanisms: (i) actual lateral rates may slow at these locations as vertical movement vectors become more dominant near the mixing transition; (ii) apparent horizontal velocities may be 'diluted' over successively larger areas as material moves outward from the NSC centre, necessitating lower apparent velocities to maintain the same rates of mass flux; and (iii) the mass flux of soil in an NSC may not be a closed system, that is, not all the material translocated to the sides on the surface may be returned to the inner domain through subsequent, recurring subduction.

CONCLUSIONS

This study is the first to utilise a powerful suite of geochemical tracers to analyse patterns and rates of material movement in a single NSC. By applying analytical and numerical models to our observed tracer distributions and inventories, we provide the primary constraints on NSC dynamics across a range of timescales at a single site.

Although our tracer suite allowed us to produce constraints on the apparent rates and patterns of cryoturbation in this particular NSC, many questions remain. Our sampling scheme and study design could not conclusively resolve whether material subduction at the inner domain edge is a continuous or stochastic process. The discontinuous form of cryoturbated materials of inferred surficial origin suggests some irregularity to the process, although this could occur either during material subduction or because of diapirism. Previous work on diapirism indicates that it would be an occasional, episodic process, although its relative importance in NSC circulation is unknown. Clear indications of stochasticity would include wide variations in ^{10}Be inventories along the direction of subducted material movement, and denser spatial information such as a fully gridded sampling scheme would be necessary to evaluate this mechanism. Resolving these questions is critical to providing an empirical foundation for the climate sensitivity of cryoturbation in NSCs and the importance of cryoturbation in the genesis of high-latitude carbon stocks over periods of centuries to millennia.

We expect that the approach presented here, when combined with detailed morphological and gridded sampling to better define small-scale changes in distributions across broad climatic gradients, will enable progress on unresolved questions related to material movement patterns and the climate sensitivity of cryoturbation rates in Arctic patterned ground.

ACKNOWLEDGEMENTS

This work was supported by a National Science Foundation DOI:10.13039/100000001 Graduate Research Fellowship to N.J. AMS DOI:10.13039/100005498 analysis of soil samples for ^{10}Be was generously provided by a Seed Grant from Purdue University DOI:10.13039/100006377 's PRIME Lab. K.Y. was supported by the National Science Foundation DOI:10.13039/100000001 (EAR-1253198) for the development of surface transport model. Funding for this study to J.K. was partly provided by the Swedish Research Council, project no. 2009–3282. The authors wish to extend sincere gratitude to two anonymous reviewers and *Permafrost and Periglacial Processes* editor Dr Julian Murton for their insightful comments and suggestions, which dramatically improved the manuscript.

SUPPORTING INFORMATION

Additional Supporting Information may be found online in the supporting information tab for this article.

Table S1. Isotope and elemental suite and properties.

Table S2. Elemental concentrations by depth and location.
Table S3. Correlation matrix – Kendall's tau-b w/Bonferroni correction for multiple comparisons. Numbers in bold are significant at an alpha value of < 0.05.
Table S4. Profile integrated inventories by location.
Appendix S1. Supplementary text
Figure S1. Relationships between SOC, Hg and S for all samples from the studied NSC. Boxes below diagonal show log–log relationships, boxes above diagonal show untransformed relationships. Diagonal boxes show untransformed variable distributions (inset) and transformed variable distributions.
Figure S2. Relationships between SOC, ^{210}Pb, ^{137}Cs and meteoric ^{10}Be for all samples of the studied NSC. Boxes below diagonal show log–log relationships, boxes above diagonal show untransformed relationships. Diagonal boxes show untransformed variable distributions (inset) and transformed variable distributions.
Figure S3. (A) Relationship between δ^{13}C and SOC (log-normalised) for all samples. (B) Down-profile trajectories of δ^{13}C and SOC for non-cryoturbated sampling locations (MT, OD1 and OD2). (C) Down-profile trajectories of δ^{13}C and SOC for cryoturbated sampling locations (CM and IN). (D) Trajectories of δ^{13}C and SOC for hypothesised direction of subsurface material movement and surficial return.
Figure S4. Inventory ratios of soil constituents normalised to the cumulative mass of profile CM (A) and MT (B).
Figure S5. Profile depth distributions for lead (Pb), total mercury (Hgtot), sulphur (S) and chlorine (Cl).
Figure S6. Profile depth distributions for total nitrogen (TN), phosphorous (P), sodium (Na), calcium (Ca), magnesium (Mg) and potassium (K).

REFERENCES

Ballantyne CK. 1996. Formation of miniature sorted patterns by shallow ground freezing: a field experiment. *Permafrost and Periglacial Processes* **7**: 406–424.

Barrie LA, Gregor D, Hargrave B, Lake R, Muir D, Shearer R, Tracey B, Bidleman T. 1992. Arctic contaminants: sources, occurrence and pathways. *Science of the Total Environment* **122**: 1–74. DOI:10.1016/0048-9697(92)90245-N

Becher M, Olid C, Klaminder J. 2013. Buried soil organic inclusions in non-sorted circles fields in northern Sweden: age and paleoclimatic context. *Journal of Geophysical Research: Biogeosciences* **118**: 104–111. DOI:10.1002/jgrg.20016

Bierman PR, Corbett LB, Graly JA, Neumann TA, Lini A, Crosby BT, Rood DH. 2014. Preservation of a preglacial landscape under the center of the Greenland ice sheet. *Science* **344**: 402–405. DOI:10.1126/science.1249047

Bindler R. 2003. Estimating the natural background atmospheric deposition rate of mercury utilizing ombrotrophic bogs in southern Sweden. *Environmental Science and Technology* **37**: 40–46. DOI:10.1021/es020065x

Bockheim JG. 2007. Importance of cryoturbation in redistributing organic carbon in permafrost-affected soils. *Soil Science Society of America Journal* **71**: 1335–1342. DOI:10.2136/sssaj2006.0414N

Daanen RP, Misra D, Epstein H, Walker D, Romanovsky VE. 2008. Simulating nonsorted circle development in Arctic tundra ecosystems. *Journal of Geophysical Research* **113**: G03S06. DOI:10.1029/2008JG000682

Dyke AS, Zoltai SC. 1980. Radiocarbon-dated mudboils, Central Canadian Arctic. *Geological Survey of Canada, Current Research, Part B* **80**: 271–275.

Ebert K, Willenbring JK, Norton KP, Hall A, Hättestrand C. 2012. Meteoric ^{10}Be concentrations from saprolite and till in northern Sweden: implications for glacial erosion and age. *Quaternary Geochronology* **12**: 11–22. DOI:10.1016/j.quageo.2012.05.005

Egginton PA, Shilts WW. 1978. Rates of movement associated with mud boils, central district of Keewatin. *Geological Survey of Canada*; 203–206 (Paper 78–01B).

Faure G, Mensing TM. 2005. Isotopes: Principles and Applications. John Wiley & Sons: Hoboken, NJ, USA.

Finkel RC, Nishiizumi K. 1997. Beryllium-10 concentrations in the Greenland Ice Sheet Project 2 ice core from 3 to 40 ka. *Journal of Geophysical Research: Oceans* **102**: 26699–26706. DOI:10.1029/97JC01282

Gee GW, Or D. 2002. The solid phase. In Methods of Soil Analyses: Part 4. Physical Methods, Dane JH, Topp GC (eds). Soil Science Society of America: Madison, WI, USA; 210–414.

Hagedorn B, Aalto R, Sletten RS, Hallet B. 2008. Frost boil dynamics using ^{210}Pb as a tracer for soil movement. In Proceedings of the Ninth International Conference on Permafrost – Fairbanks, Alaska; 613–618.

Hallet B, Anderson S, Stubbs CW, Gregory EC. 1988. Surface soil displacements in sorted circles, western Spitsbergen. In *Proceedings of the Fifth International Conference on Permafrost – Trondheim, Norway*, August 1988; 770–775.

Hallet B, Prestrud S. 1986. Dynamics of periglacial sorted circles in western Spitsbergen. *Quaternary Research* **26**: 81–99. DOI:10.1016/0033-5894(86)90085-2

Harris SA. 1998. Nonsorted circles on plateau mountain, SW Alberta, Canada. In *Proceedings of the 7th International Conference on Permafrost*. Yellowknife, CA; 441–448.

Hugelius G, Strauss J, Zubrzycki S, Harden JW, Schuur EAG, Ping C-L, Schirrmeister L, Grosse G, Michaelson GJ, Koven CD, O'Donnell JA, Elberling B, Mishra U, Camill P, Yu Z, Palmtag J, Kuhry P. 2014. Estimated stocks of circumpolar permafrost carbon with quantified uncertainty ranges and identified data gaps. *Biogeosciences* **11**: 6573–6593. DOI:10.5194/bg-11-6573-2014

Jelinski NA. 2013. Cryoturbation in the central Brooks Range, Alaska. *Soil Horizons* **54**: 01–007. DOI:10.2136/sh13-01-0006

Kääb A, Girod L, Berthling I. 2013. Surface kinematics of periglacial sorted circles using structure-from-motion technology. *The Cryosphere* **8**: 1041–1056.

Kaiser C, Meyer H, Biasi C, Rusalimova O, Barsukov P, Richter A. 2007. Conservation of soil organic matter through cryoturbation in Arctic soils in Siberia. *Journal of Geophysical Research* **112**: G02017. DOI:10.1029/2006JG000258

Klaminder J, Bindler R, Rydberg J, Renberg I. 2008. Is there a chronological record of atmospheric mercury and lead deposition preserved in the mor layer (O-horizon) of boreal forest soils? *Geochimica et Cosmochimica Acta* **72**: 703–712. DOI:10.1016/j.gca.2007.10.030

Klaminder J, Yoo K, Olid C, Ramebäck H, Vesterlund A. 2014. Using short-lived radionuclides to estimate rates of soil motion in frost boils. *Permafrost and Periglacial Processes* **25**: 184–193. DOI:10.1002/ppp.1811

Klaus M, Becher M, Klaminder J. 2013. Cryogenic soil activity along bioclimatic gradients in northern Sweden: insights from eight different proxies. *Permafrost and Periglacial Processes* **24**: 210–223. DOI:10.1002/ppp.1778

Koven C, Friedlingstein P, Ciais P, Khvorostyanov D, Krinner G, Tarnocai C.

2009. On the formation of high-latitude soil carbon stocks: effects of cryoturbation and insulation by organic matter in a land surface model. *Geophysical Research Letters* **36**: L21501. DOI:10.1029/2009GL040150

Koven CD, Ringeval B, Friedlingstein P, Ciais P, Cadule P, Khvorostyanov D, Krinner G, Tarnocai C. 2011. Permafrost carbon-climate feedbacks accelerate global warming. *Proceedings of the National Academy of Sciences of the United States of America* **108**: 14769–14774. DOI:10.1073/pnas.1103910108

Lundqvist J. 2004. Glacial history of Sweden. In Quaternary Glaciations – Extent and Chronology, Ehlers J, Gibbard PL (eds). Elsevier: Amsterdam; 401–412.

Mackay JR. 1980. The origin of hummocks, western Arctic coast, Canada. *Canadian Journal of Earth Sciences* **17**: 996–1006. DOI:10.1139/e80-100

Makoto K, Klaminder J. 2012. The influence of non-sorted circles on species diversity of vascular plants, bryophytes and lichens in sub-Arctic Tundra. *Polar Biology* **35**: 1659–1667. DOI:10.1007/s00300-012-1206-3

Miller WP, Miller DM. 1987. A micro-pipette method for soil mechanical analysis. *Communications in Soil Science and Plant Analysis* **18**: 1–15. DOI:10.1080/00103628709367799

Munthe J, Wängberg I, Rognerud S, Fjeld E, Verta M, Porvari P, Meili M. 2007. Mercury in Nordic Ecosystems. Göteborg, Sweden: IVL Swedish Environmental Research Institute, Ltd.

Nicolsky DJ, Romanovsky VE, Tipenko GS, Walker DA. 2008. Modeling biogeophysical interactions in nonsorted circles in the Low Arctic. *Journal of Geophysical Research* **113**: G03S05.

Peterson RA, Krantz WB. 2003. A mechanism for differential frost heave and its implications for patterned-ground formation. *Journal of Glaciology* **49**: 69–80. DOI:10.3189/172756503781830854

Ping CL, Jastrow JD, Jorgenson MT, Michaelson GJ, Shur YL. 2015. Permafrost soils and carbon cycling. *The Soil* **1**: 147–171. DOI:10.5194/soil-1-147-2015

Ping C-L, Michaelson GJ, Kimble JM, Romanovsky VE, Shur YL, Swanson DK, Walker DA. 2008. Cryogenesis and soil fromation along a bioclimate gradient in Arctic North America. *Journal of Geophysical Research* **113**: G03S12. DOI:10.1029/2008JG000744

Reimer PJ, Bard E, Bayliss A, Beck JW, Blackwell PG, Ramsey CB, Buck CE, Cheng H, Edwards RL, Friedrich M, Grootes PM, Guilderson TP, Haflidason H, Hajdas I, Hatté C, Heaton TJ, Hoffmann DL, Hogg AG, Hughen KA, Kaiser KF, Kromer B, Manning SW, Niu M, Reimer RW, Richards DA, Scott EM, Southon JR, Staff RA, Turney CSM, van der Plicht J. 2013. IntCal13 and Marine13 radiocarbon age calibration curves 0–50,000 years cal BP. *Radiocarbon* **55**: 1869–1887. DOI:10.2458/azu_js_rc.55.16947

Romanovsky VE, Marchenko SS, Daanen R, Sergeev DO, Walker DA. 2008. Soil climate and frost heave along the permafrost/ecological North American Arctic transect. In *Proceedings of the Ninth International Conference on Permafrost – Fairbanks, Alaska*, 29 June; 1519–1524.

Sawyer CF. 2007. Frost heaving and surface clast movement in turf-banked terraces, Eastern Glacier National Park, Montana. PhD Dissertation, Texas State University – San Marcos.

Selkirk JM. 1998. Active vegetation-banked terraces on Macquarie Island. *Zeitschrift für Geomorphologie* **42**: 483–496.

Shilts WW. 1978. Nature and genesis of mudboils, central Keewatin, Canada. *Canadian Journal of Earth Sciences* **15**: 1053–1068. DOI:10.1139/e78-113

Smith DJ. 1986. Patterned ground activity in the Mt. Rae area, southern Canadian Rocky Mountians, 1977–1985. In Current Research by Western Canadian Geographers: The University Of Alberta Papers, Jackson EL (ed). Tantalus Research Limited: Vancouver; 99–111.

Swanson DK, Ping C-L, Michaelson GJ. 1999. Diapirism in soils due to thaw of ice-rich material near the permafrost table. *Permafrost and Periglacial Processes* **10**: 349–367. DOI:10.1002/(SICI)1099-1530(199910/12)10:4<349::AID-PPP318>3.0.CO;2-N

Tarnocai C, Canadell JG, Schuur EAG, Kuhry P, Mazhitova G, Zimov S. 2009. Soil organic carbon pools in the northern circumpolar permafrost region. *Global Biogeochemical Cycles* **23**: GB2023. DOI:10.1029/2008GB003327

Trumbore S. 2009. Radiocarbon and soil carbon dynamics. *Annual Review of Earth and Planetary Sciences* **37**: 47–66. DOI:10.1146/annurev.earth.36.031207.124300

Walker DA, Epstein HE, Gould WA, Kelley AM, Kade AN, Knudson JA, Krantz WB, Michaelson G, Peterson RA, Ping C-L, Raynolds MK, Romanovsky VE, Shur YL. 2004. Frost-boil ecosystems: complex interactions between landforms, soils, vegetation and climate. *Permafrost and Periglacial Processes* **15**: 171–188. DOI:10.1002/ppp.487

Willenbring JK, von Blanckenburg F. 2010. Meteoric cosmogenic beryllium-10 adsorbed to river sediment and soil: applications for Earth-surface dynamics. *Earth-Science Reviews* **98**: 105–122. DOI:10.1016/j.earscirev.2009.10.008

Xu C, Guo L, Ping C-L, White DM. 2009. Chemical and isotopic characterization of size-fractionated organic matter from cryoturbated tundra soils, northern Alaska. *Journal of Geophysical Research* **114**: G03002. DOI:10.1029/2008JG000846